Post-processing of face-on radiographic images for quantitative analysis in ablative Rayleigh-Taylor instability experiments

L. Ceurvorst, S.F. Khan, C. Mailliet, D.A. Martinez, N. Izumi, P. Di Nicola, J.M. Di Nicola, T. Goudal, V. Bouffetier, D. Kalantar, et al.

Version of Record: https://www.sciencedirect.com/science/article/pii/S1574181820300914
Manuscript_696588e7121ee9ab797a788835e678b4

Post-processing of face-on radiographic images for quantitative analysis in ablative Rayleigh-Taylor instability experiments

L. Ceurvorst,[1] S. F. Khan,[2] C. Mailliet,[1] D.A. Martinez,[2] N. Izumi,[2] P. Di Nicola,[2] J.M. Di Nicola,[2] T. Goudal,[1] V. Bouffetier,[1] D. Kalantar,[2] I. Igumenshchev,[3] E. Le Bel,[1] B.A. Remington,[2] L. P. Masse,[2] V.A. Smalyuk,[2] and A. Casner[1]

[1]*Université de Bordeaux-CNRS-CEA, Centre Lasers Intenses et Applications (CELIA), UMR 5107, F-33405 Talence, France*
[2]*Lawrence Livermore National Laboratory, Livermore, CA 94550, USA*
[3]*Laboratory for Laser Energetics, University of Rochester, 250 E. River Rd, Rochester, NY 14623, USA*

An experiment was performed at the National Ignition Facility investigating the ablative Rayleigh-Taylor instability's dependence on initial conditions in the highly nonlinear stage. The detailed post-processing of the radiographic images which includes backlighter reconstruction, Wiener deconvolution of the raw data, and the calculation of a conversion factor from optical depth to physical units. The results of these calculations were fed into the primary analysis of the experimental data, with this manuscript serving as a supplemental reference to the primary paper [1].

The Rayleigh-Taylor instability (RTI) [2, 3] occurs at the interface of two fluids and is one of the most ubiquitous hydrodynamic instabilities. It can be seen in astronomical formations such as supernovae explosions [4–7] and nebulae [8, 9], in Bose-Einstein condensates [10] including granular material problems [11], and in inertial confinement fusion (ICF) [12]. Yet despite its prevalence and the great deal of research focused on understanding the RTI since Lord Rayleigh's seminal paper, its behavior is still not fully understood [13].

When one fluid is accelerated against a heavier fluid, or in other words, when the acceleration of the interface is opposed to its density gradient, the RTI causes any perturbations on the interface to grow exponentially according to the Betti-Takabe growth rate [14]:

$$\gamma = \alpha\sqrt{\frac{kg}{1+kL_{\text{min}}}} - \beta k V_a \tag{1}$$

where $\alpha = 0.98$ and $\beta = 1.7$ for CH targets, $k = 2\pi/\lambda$ is the wavenumber of the perturbations, λ the perturbation wavelength, g the acceleration of the interface, L_{min} the minimum scale length of the density profile between the two fluids, and V_a the ablation velocity. Thus, its evolution is strongly dependent on the initial perturbations. The source of these perturbations may come from initial target defects [15] or, in the case of laser-driven experiments, from non-uniformities in the incident laser beams [16]. Speckles in the beam's spatial intensity profile are imprinted onto a target, resulting in mass-density perturbations [17–19]. These then act as seeds for the RTI on what may have otherwise been a smooth target.

These seeds will grow exponentially until their amplitudes approach their transverse size. Once this occurs, nonlinearities such as the Kelvin-Helmholtz instability grow along the interface [20–22]. This causes the instability to cease growing exponentially and shift into a constant velocity state wherein light fluid bubbles will push into the heavy fluid while heavy spikes penetrate deeper into the lighter fluid. The amplitude at which this shift occurs is predicted by Haan's theory [23] and is proportional to the area of the bubble. Thus, smaller bubbles will saturate at lower amplitudes while larger bubbles will saturate much later.

This nonlinear regime is dominated by two processes: bubble competition and bubble merger [20, 21]. Competition occurs when small-wavelength bubbles saturate and continue growing at a linear rate. These are quickly overtaken by larger bubbles which continue their exponential growth well past these amplitudes. Merger, on the other hand, occurs when two similarly sized bubbles nonlinearly couple together to form a single larger bubble. If an interface consists primarily of similarly sized modulations, bubble merger will therefore be the dominant effect. Similarly, if a range of wavelengths are present, competition may take over. Both of these processes result in a shift in the perturbation spectrum towards longer wavelengths, and both are predicted to yield a self-similarity wherein the bubble heights, h_b, are proportional to the distance traveled by the interface, $h_b = \alpha_b A_T g t^2$ where $A_T = (\rho_1 - \rho_2)/(\rho_1 + \rho_2)$ is the Atwood number, ρ_i is the mass density of fluid i, g is the acceleration of the interface, and t is time. However, the rates at which these two phenomena occur are predicted to vary [21]. As a result, different α_b measurements may be obtained depending on how dominant bubble merger versus bubble competition is. This implies that initial conditions could play a large role in the nonlinear behavior of such a system.

To this end, an experiment was performed at the National Ignition Facility (NIF) [24] using the recently

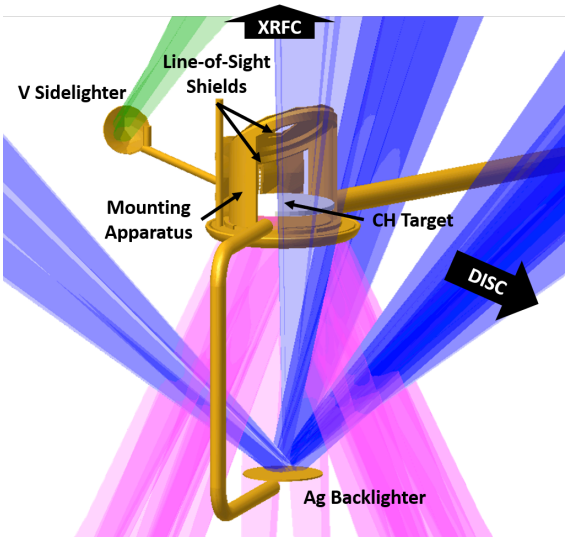

FIG. 1: Schematic of experimental setup. Magenta beams are the main drive beams, blue the backlighter beams, and green the sidelighter beam. The target's initial position is flush with the bottom of the mounting apparatus.

developed planar direct-drive platform [25–27] which builds upon previous work at smaller facilities [28]. This experiment was designed to create two different three-dimensional (3D) multimode initial surface profiles through laser imprint on smooth planar CH targets. These targets were then accelerated to unprecedentedly long travel distances with a drive laser and observed using face-on gated radiography and side-on streaked radiography. While other experiments in indirect drive have approached this regime in 2D [29], this design enabled the deeply nonlinear behavior of the ablative RTI to be directly observed for the first time ever experimentally in direct drive.

The resulting density structures in such a system quickly become extremely complex, and the density profile even just within the heavy fluid becomes highly inhomogeneous. Thus, such an experiment requires a great deal of precision in its analysis. This paper details the post-processing of the data acquired in this experiment to obtain bubble amplitudes from the face-on radiography. A full analysis of the resulting images has already been submitted for publication elsewhere [1], the results of which show for the first time experimentally that the nonlinear growth of the RTI does indeed strongly depend on the initial perturbation spectrum.

A 300 μm-thick plastic target was mounted on top of a Au washer as shown in Fig. 1. The rest of the mounting apparatus acted as line-of-sight shields for the x-ray diagnostics. The initial 3D seeds of the ablative RTI were formed using a 351 nm-wavelength imprint beam (B427 or B428, belonging to the 23.5° cone) focused onto the target at $t = -300$ ps. Modeling [18] and experiments [30] predict that this delay will maximize the imprint efficiency. No smoothing-by-spectral-dispersion (SSD) gratings were used so that the speckle patterns were constant in time. To achieve different initial conditions, the imprint beam on one target directly impinged with no smoothing techniques and was defocused by 18 mm from the target surface. The second target's beam was smoothed by a continuous phase plate (CPP) and directly focused onto the target. Equivalent target-plane images of these beams were acquired prior to the shots on the NIF target alignment sensor (TAS) and their spectra show the different profiles to be imprinted on each target. The one-dimensional (1D) Fourier spectra of these beams were calculated by azimuthally averaging the two-dimensional (2D) Fourier transform of the TAS images. The shot which used a CPP on the imprint beam, the "smoothed" shot (Fig. 2(a)), resulted in broadband features to high-frequencies beyond 100 mm^{-1} which correspond to features of ~8 μm, close to the diffraction limit of $\lambda_L f_N$ where $\lambda_L = 351$ nm is the laser wavelength and $f_N = 20.76$ is the f-number for one NIF beam. On the other hand, the features of the defocused beam without CPP smoothing, the "unsmoothed" shot (Fig. 2(b)), were much more concentrated at low frequencies with the smallest features having spatial sizes of ~16 μm. The low-frequency structure of this speckling is evident. The Betti-Takabe growth rate, given by Eq. 1, is plotted against the azimuthally binned Fourier spectra of these two speckle patterns in Fig. 2(c).

After the imprint from these beams had reached its predicted optimum levels, the now-perturbed target was accelerated using ~440 kJ of laser energy over 30 ns. This was achieved using 21 NIF quads of 351 nm laser light to irradiate the foil each as a 10 ns square pulse. These quads were split into groups of 7 and stacked in time to create the final 30 ns pulse. The grouping of beams went from the outer beams to the inner beams, refocusing deeper into the apparatus to track the target and maintain near constant acceleration. Specifically, beams from the 50° cone were focused on the target's initial position from $t = 0 - 10$ ns, followed by 44.5° beams pointed 0.75 mm behind the initial target position from 10-20 ns, and finally the inner beams (23.5° and 30°) defocused by 1.5 mm from 20-30 ns.

To observe the evolution of the system, a set of imaging diagnostics were fielded to measure the acceleration

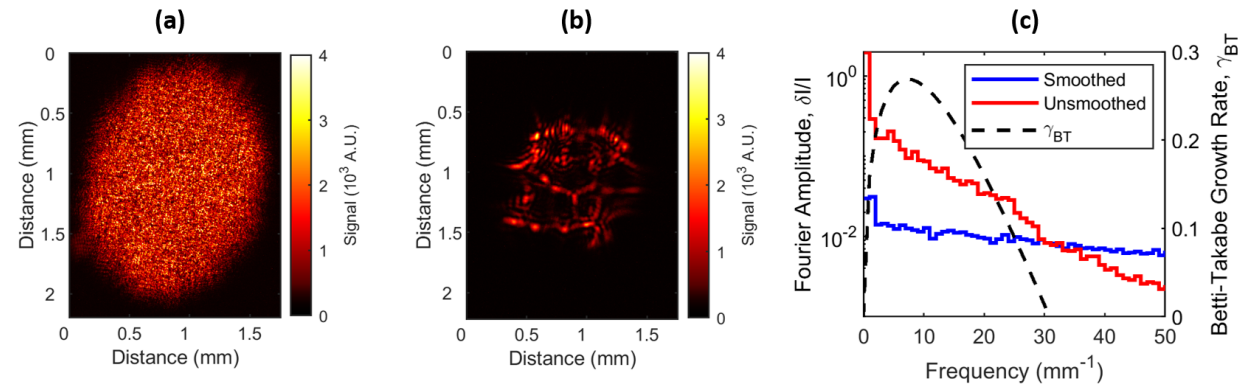

FIG. 2: The TAS images of the imprint beam for (a) the smoothed and (b) the unsmoothed shots. (c) The 2D fourier spectra of the center of these TAS images are azimuthally binned and plotted against the Betti-Takabe growth rate.

of the foil and observe the growth of the 3D RTI modulations. To track the target's position, a vanadium sidelighter was irradiated using one NIF quad, delivering 18 kJ of energy over 10 ns. The resulting x-rays had a peak intensity of 5×10^{14} W cm^{-2} at 5.2 keV photon energy and probed the target transversely. They were then collected by a DIM-Insertable Streak Camera (DISC) [31] with 12× magnification to give the target's front- and rear-surface positions against time. Meanwhile, the RTI growth was captured using through-foil face-on x-ray radiography. The x-rays for this diagnostic were produced using a silver backlighter irradiated by 9 quads with a 9 ns square pulse. This created a peak intensity of 8×10^{14} W cm^{-2} at 3.6 keV. After passing longitudinally through the target, these x-rays were imaged using a staggered array of 19 µm pinholes coupled with a four-strip gated x-ray detector (GXD) [32] and recorded using a charge-coupled device (CCD). The initial target-to-pinhole distance 110 mm and the pinhole-to-image-plane distance is 663 mm resulting in a magnification of 6.02×. The strips of the GXD were timed so that images would be captured at t = 14, 17, 20, and 23 ns. It is the post-processing of these images that is the subject of the remainder of this paper.

Fig. 3(a) shows the raw output of the GXD diagnostic for the smoothed shot with the locations and timings of each strip superimposed. While several features are clearly visible, in order to get an accurate quantitative measurement, the backlighter profile must first be inferred and then removed from each image. This is done via back-projection of the images to the backlighter plane. The longitudinal distances between the backlighter, target, pinholes, and image plane are all fixed by the experimental geometry. All that is then required to fully know the exact configuration is the 3D positioning of the pinholes. These are calculated by correlating multiple sets of features from the images together as indicated in Fig. 3(a). Since the physical pixel size of the CCD is known and the average position of these features correlates to an approximately constant position in the target plane, the pinholes' positions can be calculated through simple geometric ray tracing.

These positions may then be used to back-project each sub-image to the backlighter plane. Taking the average of these images in this plane forms a composite image of the backlighter as shown in 3(b). To remove the high-frequency features that result from the interaction of the x-rays with the target, a low-pass filter is applied and a 2D polynomial is fitted to the outside points. The resulting backlighter profile, shown in Fig. 3(c), is then forward-projected to the image plane. The absorption of the probe is given as the reconstructed backlighter profile divided by the original data. Note that the backlighter profile is reconstructed for each shot. This process only provided the shape of the backlighter – its maximum intensity will be discussed shortly.

In addition to the backlighter profile, the images collected by the CCD are blurred by the pinholes, the micro-channel plates (MCP) which form the strips of the GXD, and the CCD itself, and noise is added throughout. To remove these blurring effects and obtain a better representation of the true data, the images must be Wiener deconvolved using the process detailed in Ref. [33]. This first requires noise and signal spectra. It should be noted that the time between adjacent images on a single MCP strip is on the scale of tens of picoseconds. As a result, the hydrodynamics of the system do not have significant time to develop between these images, and they may be

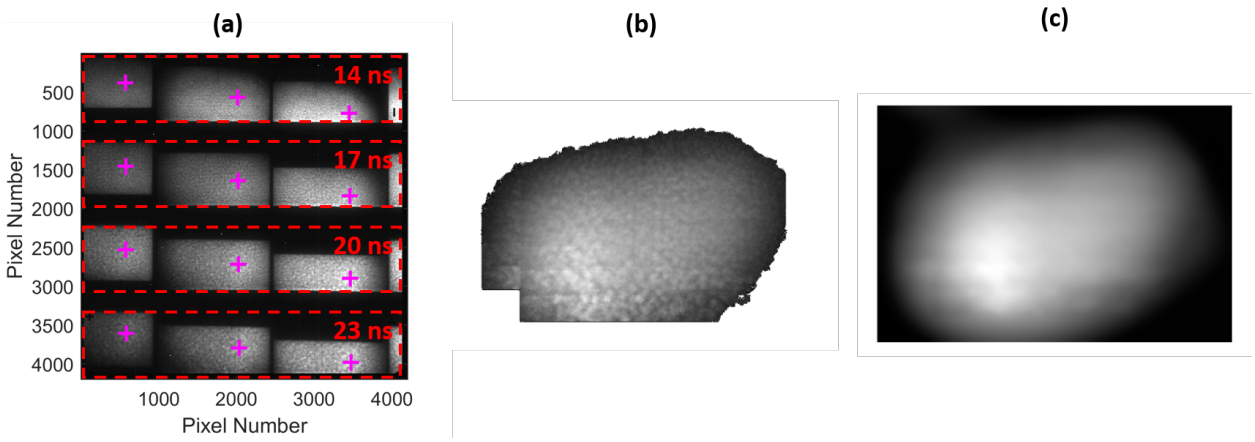

FIG. 3: The backlighter reconstruction process. (a) The raw data for the smooth shot is presented. Superimposed dashed red rectangles show the location of the GXD strips with their corresponding times. The magenta reticles show an example set of correlated features used to determine the pinhole positions. (b) The average of all twelve back-projected images in the backlighter's plane. (c) The final backlighter profile used for the smooth shots after applying a low-pass filter and fitting a polynomial to the edges of the average back-projected image.

treated as nearly identical. These images can then be correlated together, and overlapping regions can either be added or subtracted from one another to form approximate noise and signal images as shown in Fig. 4. The modulated transfer function (MTF) of this system has been previously well-characterized. The procedure described in Ref. [33] may now be followed to remove the blurring effects and reduce noise of these images.

These deconvolved images may now be used to determine the optical depth (OD), given simply by the natural logarithm of the reconstructed backlighter divided by the deconvolved images. The amplitude of the backlighter for each image was chosen so that the resulting OD images are equal to zero in the unperturbed portions of the target such as those present in the bottom corners of Fig. 4(a). This implies that bubbles, where the target is thinner and less absorption occurs, will have negative OD values while spikes will be positive. The final result of this is shown in Fig. 5. Note that due to the nature of the calculation, noise has been drastically suppressed and high-frequency structures have been enhanced due to the deconvolution.

As stated in the introduction, the goal of this experiment was to observe the growth of the RTI bubbles. This requires a conversion from OD to physical height. These two are related through the equation $\tau = \int_0^h \mu\rho(z)dz$ where τ is the OD, h the height, μ the mass attenuation coefficient, and $\rho(z)$ the density as a function of longitudinal position, z. When ρ is approximately constant, $\rho(z) \approx \rho_0$, this simplifies to $h = \tau/\mu\rho_0$. However, this assumption does not hold in the nonlinear phase of the RTI [34]. Further, the temperature of the material is expected to reach several hundred eV, making cold μ measurements inapplicable. Instead, a new method must be developed to convert from OD to height.

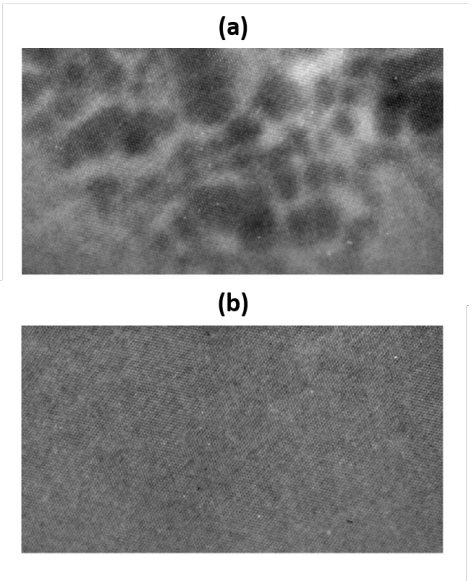

FIG. 4: (a) Signal and (b) noise images created by taking the average sum and difference respectively of two correlated regions from the $t = 17$ ns strip of the unsmoothed shot.

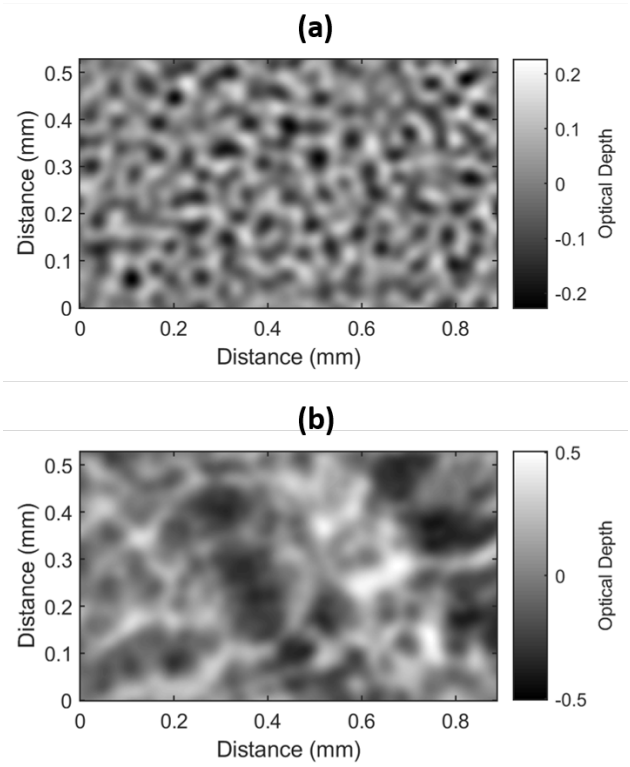

FIG. 5: Fully post-processed OD images for (a) the smoothed and (b) unsmoothed shots 17 ns after the start of the main drive.

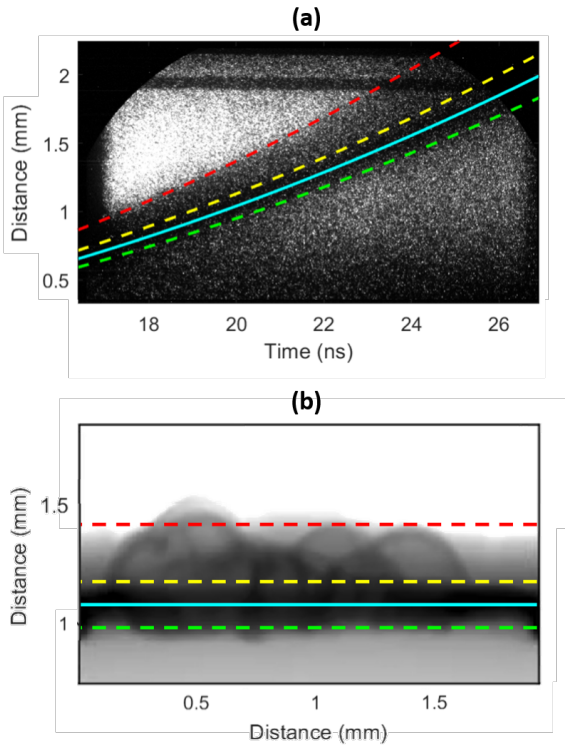

FIG. 6: (a) The streaked sidelighter image for the unsmoothed shot showing the target's trajectory. The three edges in brightness have been fit with parabolas, shown with dashed lines. The solid cyan line is the average of the yellow and green dashed lines and indicates the unperturbed target's mean position. (b) Artificial side-on radiography of the HYDRA-simulated unsmoothed target at $t = 17.4$ ns. The superimposed lines correlate the features shown in this image to the DISC image in (a). The laser drive is incident from the bottom of both windows.

In the unsmoothed shot, the side-on streaked radiography showed two distinct regions within the target — one dark region and one which still transmitted some signal (see Fig. 6(a)). To better understand this result, a full-scale simulation was run in the arbitrary-Lagrangian-Eulerian radiation-hydrodynamics code, HYDRA [35, 36]. This simulation included realistic unsmoothed imprint beam profiles with 200,000 rays per beam and matched the experimental conditions presented above. The 8 mm window had a 25 µm base resolution with an increased 6 µm resolution in the central 2 mm square where the imprint took place. Their output was post-processed to form both face-on and side-on gated x-ray radiographic images. Fig. 6(b) shows the side-on image for this simulation after 17.4 ns of drive. While the growth of the RTI is overestimated due to resolution limitations creating oversized initial seeds, the artificial radiographs are descriptive. Bubbles in the unsmoothed shot extended beyond the rear surface of the unperturbed target. Since the radiographs are integrated through the entire target, the large unperturbed region which is not subject to significant RTI growth absorbs virtually all x-rays passing through it, creating the darkest strip of this radiograph. The thinner bubble region beyond this rear surface contains far less mass, and as a result, some portion of the incident photons are still able to penetrate through this region. This matches what is seen in the experimental side-on streaked radiography. Thus the edge traced in red in Fig. 6(a) represents the maximum bubble height. Simulations show that the spikes remain near the unperturbed material's front surface. However, this is impossible to verify from the experimental data. Instead, the deepest spike position is taken to be in the middle of the unperturbed region,

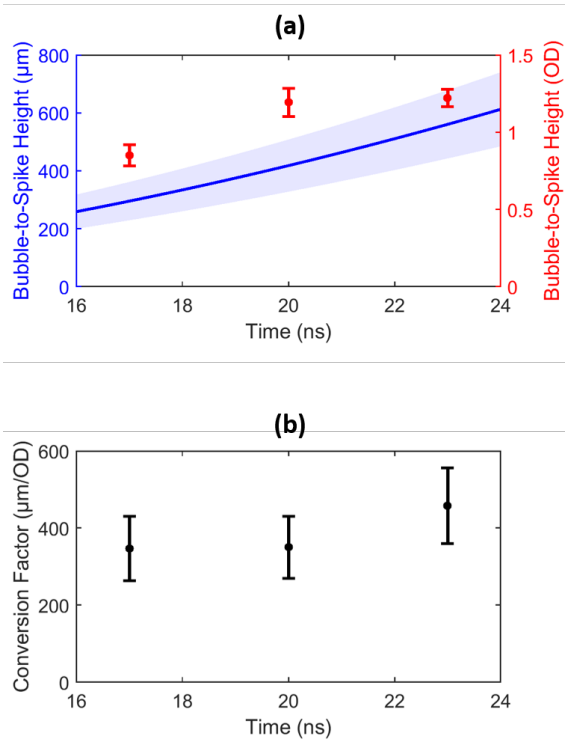

FIG. 7: (a) The maximum bubble-to-spike height in microns extracted from the sidelighter's fitted curves is shown in blue. The light-blue shaded region indicates the error due to the uncertain spike position within the unperturbed region. The red plot shows the maximum bubble-to-spike height from the face-on radiography in OD. (b) The ratio of these two gives the final conversion factor. Note that The plateauing of the OD bubble-to-spike height in (a) and the subsequent increased conversion factor in (b) at $t = 23$ ns is due to perforation of the target.

shown in cyan in Fig. 6(a), with an uncertainty equal to half of this region's width.

Finally, to determine the average conversion factor from OD to physical height, the distance between these maximum bubble and spike positions is compared to the difference between the maximum and minimum OD in the processed face-on images at $t = 17$ ns and 20 ns. The streaked radiograph didn't begin until approximately $t = 17$ ns, and various measurements suggested that the target had perforated by 23 ns as demonstrated in Ref. [1]. As a result, these two timesteps were excluded from the analysis. However, the central two times produced extremely consistent conversion factors as shown in Fig. 7. These result in a final average conversion factor from OD to physical height of 320 ± 90 μm/OD.

In conclusion, an experiment was performed at the NIF to investigate the highly nonlinear stages of the RTI. In order to obtain a quantitative analysis of the results, several post-processing steps had to first be carried out. Face-on gated radiographs were obtained and post-processed by reconstructing the backlighter profile, Wiener deconvolved and converted to OD. A comparison to the side-on streaked target trajectories was used to gain a rough approximation of the conversion factor from OD to physical height which was consistent between measurements. The results of this post-processing fed into the full quantitative analysis of the experiment and informed the physical interpretation of the results.

We gratefully acknowledge the access to the NIF facility for the basic science experiments described herein, which was through the NIF Discovery Science program, which issues an annual call for proposals for basic science experiments on NIF. A.C., C.M. and L.C. acknowledge funding from CEA DAM.

[1] L. Ceurvorst, S. F. Khan, C. Mailliet, D. A. Martinez, N. Izumi, P. Di Nicola, J. M. Di Nicola, T. Goudal, V. Bouffetier, D. Kalantar, I. Igumenshchev, E. Le Bel, B. A. Remington, L. P. Masse, V. A. Smalyuk, and A. Casner, "Dependence on initial conditions for the ablative Rayleigh-Taylor Instability in the highly nonlinear regime," To be published.
[2] L. Rayleigh, *Scientific papers* (Cambridge University Press Vol II, 1900).
[3] G. I. Taylor, Proceedings of the Royal Society of London. Series A. Mathematical and Physical Sciences **201**, 192 (1950).
[4] W. H. Cabot and A. W. Cook, Nature Physics **2**, 562 (2006).
[5] E. P. Hicks, The Astrophysical Journal **803**, 72 (2015).
[6] P. C. Duffell and D. Kasen, The Astrophysical Journal **842**, 18 (2017).
[7] K. Kifonidis, T. Plewa, H.-T. Janka, and E. Müller, Astronomy & Astrophysics **408**, 621 (2003), arXiv:0302239 [astro-ph].
[8] H. Zhang, R. Betti, R. Yan, D. Zhao, D. Shvarts, and H. Aluie, Physical Review Letters **121**, 185002 (2018).
[9] E. Frieman, Ap. J. **120**, 18 (1954).
[10] K. Sasaki, N. Suzuki, D. Akamatsu, and H. Saito, Physical Review A **80**, 063611 (2009).
[11] J. L. Vinningland, O. Johnsen, E. G. Flekkøy, R. Toussaint, and K. J. Måløy, Phys. Rev. Lett. **99**, 048001 (2007).
[12] B. A. Remington, H.-S. Park, D. T. Casey, R. M. Cavallo, D. S. Clark, C. M. Huntington, C. C. Kuranz, A. R. Miles, S. R. Nagel, K. S. Raman, and V. A. Smalyuk, Proceedings of the National Academy of Sciences **116**, 18233 (2019),

https://www.pnas.org/content/116/37/18233.full.pdf.
[13] P. Ramaprabhu, G. Dimonte, P. Woodward, C. Fryer, G. Rockefeller, K. Muthuraman, P.-H. Lin, and J. Jayaraj, Physics of Fluids **24**, 074107 (2012).
[14] R. Betti, V. N. Goncharov, R. L. McCrory, and C. P. Verdon, Phys. Plasmas **5**, 1446 (1998).
[15] J. P. Knauer, R. Betti, D. K. Bradley, T. R. Boehly, T. J. B. Collins, V. N. Goncharov, P. W. McKenty, D. D. Meyerhofer, V. A. Smalyuk, C. P. Verdon, S. G. Glendinning, D. H. Kalantar, and R. G. Watt, Physics of Plasmas **7**, 338 (2000).
[16] V. A. Smalyuk, O. Sadot, R. Betti, V. N. Goncharov, J. A. Delettrez, D. D. Meyerhofer, S. P. Regan, T. C. Sangster, and D. Shvarts, Physics of Plasmas **13**, 056312 (2006).
[17] S. P. Regan, D. K. Bradley, A. V. Chirokikh, R. S. Craxton, D. D. Meyerhofer, W. Seka, R. W. Short, A. Simon, R. P. J. Town, B. Yaakobi, J. J. Carroll, and R. P. Drake, Physics of Plasmas **6**, 2072 (1999).
[18] V. N. Goncharov, O. V. Gotchev, E. Vianello, T. R. Boehly, J. P. Knauer, P. W. McKenty, P. B. Radha, S. P. Regan, T. C. Sangster, S. Skupsky, V. A. Smalyuk, R. Betti, R. L. McCrory, D. D. Meyerhofer, and C. Cherfils-Clérouin, Physics of Plasmas **13**, 012702 (2006).
[19] D. A. Martinez, V. A. Smalyuk, I. V. Igumenshchev, B. Delorme, A. Casner, L. Masse, H.-S. Park, B. A. Remington, and M. Olazabal-Loumé, Physics of Plasmas **24**, 102702 (2017).
[20] P. Ramaprabhu, G. Dimonte, and M. J. Andrews, Journal of Fluid Mechanics **536**, 285 (2005).
[21] D. L. Youngs, Philosophical Transactions of the Royal Society A: Mathematical, Physical and Engineering Sciences **371**, 20120173 (2013).
[22] P. Ramaprabhu, G. Dimonte, P. Woodward, C. Fryer, G. Rockefeller, K. Muthuraman, P.-H. Lin, and J. Jayaraj, Physics of Fluids **24**, 074107 (2012).
[23] S. W. Haan, Phys. Rev. A **39**, 5812 (1989).
[24] E. Moses, R. Boyd, B. A. Remington, C. J. Keane, and R. Al-Ayat, Phys. Plasmas **16** (2009).
[25] A. Casner, C. Mailliet, S. F. Khan, D. Martinez, N. Izumi, D. Kalantar, P. D. Nicola, J. M. D. Nicola, E. L. Bel, I. Igumenshchev, V. T. Tikhonchuk, B. A. Remington, L. Masse, and V. A. Smalyuk, Plasma Physics and Controlled Fusion **60**, 014012 (2018).
[26] A. Casner, C. Mailliet, G. Rigon, S. Khan, D. Martinez, B. Albertazzi, T. Michel, T. Sano, Y. Sakawa, P. Tzeferacos, D. Lamb, S. Liberatore, N. Izumi, D. Kalantar, P. D. Nicola, J. D. Nicola, E. L. Bel, I. Igumenshchev, V. Tikhonchuk, B. Remington, J. Ballet, E. Falize, L. Masse, V. Smalyuk, and M. Koenig, Nuclear Fusion **59**, 032002 (2018).
[27] C. Mailliet, E. Le Bel, L. Ceurvorst, S. F. Khan, D. Martinez, T. Goudal, N. Izumi, D. Kalantar, P. Di Nicola, J. M. Di Nicola, I. Igumenshchev, V. T. Tikhonchuk, B. Remington, V. A. Smalyuk, L. Masse, and A. Casner, Physics of Plasmas **26**, 082703 (2019), https://doi.org/10.1063/1.5110684.
[28] V. A. Smalyuk, O. Sadot, J. A. Delettrez, D. D. Meyerhofer, S. P. Regan, and T. C. Sangster, Phys. Rev. Lett. **95**, 215001 (2005).
[29] D. A. Martinez, V. A. Smalyuk, I. V. Igumenshchev, B. Delorme, A. Casner, L. Masse, H.-S. Park, B. A. Remington, and M. Olazabal-Loumé, Physics of Plasmas **24**, 102702 (2017).
[30] V. A. Smalyuk, V. N. Goncharov, T. R. Boehly, J. A. Delettrez, D. Y. Li, J. A. Marozas, A. V. Maximov, D. D. Meyerhofer, S. P. Regan, and T. C. Sangster, Physics of Plasmas **12**, 072703 (2005).
[31] Y. P. Opachich, D. H. Kalantar, A. G. MacPhee, J. P. Holder, J. R. Kimbrough, P. M. Bell, D. K. Bradley, B. Hatch, G. Brienza-Larsen, C. Brown, C. G. Brown, D. Browning, M. Charest, E. L. Dewald, M. Griffin, B. Guidry, M. J. Haugh, D. G. Hicks, D. Homoelle, J. J. Lee, A. J. Mackinnon, A. Mead, N. Palmer, B. H. Perfect, J. S. Ross, C. Silbernagel, and O. Landen, Review of Scientific Instruments **83**, 125105 (2012).
[32] G. A. Kyrala, S. Dixit, S. Glenzer, D. Kalantar, D. Bradley, N. Izumi, N. Meezan, O. L. Landen, D. Callahan, S. V. Weber, J. P. Holder, S. Glenn, M. J. Edwards, P. Bell, J. Kimbrough, J. Koch, R. Prasad, L. Suter, J. L. Kline, and J. Kilkenny, Rev. Sci. Instrum. **81**, 10E316 (2010).
[33] V. A. Smalyuk, T. R. Boehly, D. K. Bradley, J. P. Knauer, and D. D. Meyerhofer, Review of Scientific Instruments **70**, 647 (1999).
[34] G. Dimonte, Phys. Rev. E **69**, 056305 (2004).
[35] M. M. Marinak, B. A. Remington, S. V. Weber, R. E. Tipton, S. W. Haan, K. S. Budil, O. L. Landen, J. D. Kilkenny, and R. Wallace, Phys. Rev. Lett. **75**, 3677 (1995).
[36] M. M. Marinak, S. G. Glendinning, R. J. Wallace, B. A. Remington, K. S. Budil, S. W. Haan, R. E. Tipton, and J. D. Kilkenny, Phys. Rev. Lett. **80**, 4426 (1998).